Spectral measurement of the ^{214}Bi β decay to the ^{214}Po ground state with the XENONnT Experiment

E. Aprile,[1] J. Aalbers,[2] K. Abe,[3] M. Adrover,[4] S. Ahmed Maouloud,[5] L. Althueser,[6] B. Andrieu,[5] E. Angelino,[7] D. Antón Martin,[8] S. R. Armbruster,[9] F. Arneodo,[10] L. Baudis,[4] M. Bazyk,[11] L. Bellagamba,[12] R. Biondi,[13,7] A. Bismark,[4] K. Boese,[9] R. M. Braun,[6] A. Brown,[14] G. Bruno,[11] R. Budnik,[13] C. Cai,[15] C. Capelli,[4] J. M. R. Cardoso,[16] A. P. Cimental Chávez,[4] A. P. Colijn,[17] J. Conrad,[18] J. J. Cuenca-García,[4] V. D'Andrea,[7,*] L. C. Daniel Garcia,[5] M. P. Decowski,[17] A. Deisting,[19] C. Di Donato,[20,7] P. Di Gangi,[12] S. Diglio,[11] K. Eitel,[21] S. el Morabit,[17] R. Elleboro,[20] A. Elykov,[21] A. D. Ferella,[20,7] C. Ferrari,[7] H. Fischer,[14] T. Flehmke,[18] M. Flierman,[17] D. Fuchs,[18] W. Fulgione,[22,7] C. Fuselli,[17,†] R. Gaior,[5] F. Gao,[15] R. Giacomobono,[23] F. Girard,[5] R. Glade-Beucke,[14] L. Grandi,[8] J. Grigat,[14] H. Guan,[24] M. Guida,[9] P. Gyorgy,[19] R. Hammann,[9] A. Higuera,[25] C. Hils,[19] L. Hoetzsch,[4,9] N. F. Hood,[26] M. Iacovacci,[23] Y. Itow,[27] J. Jakob,[6] F. Joerg,[4] Y. Kaminaga,[3] M. Kara,[21] S. Kazama,[27] P. Kharbanda,[17] M. Kobayashi,[27] D. Koke,[6] K. Kooshkjalali,[19] A. Kopec,[26,‡] H. Landsman,[13] R. F. Lang,[24] L. Levinson,[13] I. Li,[25] S. Li,[28] S. Liang,[25] Z. Liang,[28] Y.-T. Lin,[6,9,§] S. Lindemann,[14] M. Lindner,[9] K. Liu,[15] M. Liu,[1] J. Loizeau,[11] F. Lombardi,[19] J. A. M. Lopes,[16,‖] G. M. Lucchetti,[12] T. Luce,[14] Y. Ma,[26] C. Macolino,[20,7] J. Mahlstedt,[18] F. Marignetti,[23] T. Marrodán Undagoitia,[9] K. Martens,[3] J. Masbou,[11] S. Mastroianni,[23] V. Mazza,[12] A. Melchiorre,[20,7] J. Merz,[19] M. Messina,[7] K. Miuchi,[29] A. Molinario,[22] S. Moriyama,[3] K. Morå,[1] M. Murra,[1] J. Müller,[14] K. Ni,[26] C. T. Oba Ishikawa,[3] U. Oberlack,[19] S. Ouahada,[4] B. Paetsch,[13] Y. Pan,[5] Q. Pellegrini,[5] R. Peres,[4] J. Pienaar,[13] M. Pierre,[17] G. Plante,[1] T. R. Pollmann,[17] A. Prajapati,[20] L. Principe,[11] J. Qin,[25] D. Ramírez García,[4] M. Rajado,[4] A. Ravindran,[11] A. Razeto,[7] R. Singh,[24] L. Sanchez,[25] J. M. F. dos Santos,[16] I. Sarnoff,[10] G. Sartorelli,[12] J. Schreiner,[9] P. Schulte,[6] H. Schulze Eißing,[6] M. Schumann,[14] L. Scotto Lavina,[5] M. Selvi,[12] F. Semeria,[12] P. Shagin,[19] S. Shi,[1] H. Simgen,[9] A. Stevens,[14] C. Szyszka,[19] A. Takeda,[3] Y. Takeuchi,[29] P.-L. Tan,[1] D. Thers,[11] G. Trinchero,[22] C. D. Tunnell,[25] F. Tönnies,[14] K. Valerius,[21] S. Vecchi,[30] S. Vetter,[21] G. Volta,[9] C. Weinheimer,[6] M. Weiss,[13] D. Wenz,[6] C. Wittweg,[4] V. H. S. Wu,[21] Y. Xing,[11] D. Xu,[1] Z. Xu,[1] M. Yamashita,[3] J. Yang,[28] L. Yang,[26] J. Ye,[31] M. Yoshida,[3] L. Yuan,[8] G. Zavattini,[30] Y. Zhao,[15] M. Zhong,[26] and T. Zhu[3]

(XENON Collaboration)[¶]

[1]*Physics Department, Columbia University, New York, New York 10027, USA*

[2]*Nikhef and the University of Groningen, Van Swinderen Institute, 9747AG Groningen, Netherlands*

[3]*Kamioka Observatory, Institute for Cosmic Ray Research, and Kavli Institute for the Physics and Mathematics of the Universe (WPI), University of Tokyo, Higashi-Mozumi, Kamioka, Hida, Gifu 506-1205, Japan*

[4]*Physik-Institut, University of Zürich, 8057 Zürich, Switzerland*

[5]*LPNHE, Sorbonne Université, CNRS/IN2P3, 75005 Paris, France*

[6]*Institut für Kernphysik, University of Münster, 48149 Münster, Germany*

[7]*INFN-Laboratori Nazionali del Gran Sasso and Gran Sasso Science Institute, 67100 L'Aquila, Italy*

[8]*Department of Physics, Enrico Fermi Institute & Kavli Institute for Cosmological Physics, University of Chicago, Chicago, Illinois 60637, USA*

[9]*Max-Planck-Institut für Kernphysik, 69117 Heidelberg, Germany*

[10]*New York University Abu Dhabi, Center for Astro, Particle and Planetary Physics, Abu Dhabi, United Arab Emirates*

[11]*SUBATECH, IMT Atlantique, CNRS/IN2P3, Nantes Université, 44307 Nantes, France*

[12]*Department of Physics and Astronomy, University of Bologna and INFN-Bologna, 40126 Bologna, Italy*

[13]*Department of Particle Physics and Astrophysics, Weizmann Institute of Science, Rehovot 7610001, Israel*

[14]*Physikalisches Institut, Universität Freiburg, 79104 Freiburg, Germany*

[15]*Department of Physics & Center for High Energy Physics, Tsinghua University, Beijing 100084, People's Republic of China*

[16]*LIBPhys, Department of Physics, University of Coimbra, 3004-516 Coimbra, Portugal*

[*]Also at INFN-Roma Tre, 00146 Roma, Italy.

[†]Contact author: cfuselli@nikhef.nl

[‡]Present address: Department of Physics & Astronomy, Bucknell University, Lewisburg, Pennsylvania, USA.

[§]Contact author: ylin3@uni-muenster.de

[‖]Also at Coimbra Polytechnic - ISEC, 3030-199 Coimbra, Portugal.

[¶]Contact author: xenon@lngs.infn.it

[17]*Nikhef and the University of Amsterdam, Science Park, 1098XG Amsterdam, Netherlands*
[18]*Oskar Klein Centre, Department of Physics, Stockholm University, AlbaNova, SE-10691 Stockholm, Sweden*
[19]*Institut für Physik & Exzellenzcluster PRISMA$^+$, Johannes Gutenberg-Universität Mainz, 55099 Mainz, Germany*
[20]*Department of Physics and Chemistry, University of L'Aquila, 67100 L'Aquila, Italy*
[21]*Institute for Astroparticle Physics, Karlsruhe Institute of Technology, 76021 Karlsruhe, Germany*
[22]*INAF-Astrophysical Observatory of Torino, Department of Physics, University of Torino and INFN-Torino, 10125 Torino, Italy*
[23]*Department of Physics "Ettore Pancini," University of Napoli and INFN-Napoli, 80126 Napoli, Italy*
[24]*Department of Physics and Astronomy, Purdue University, West Lafayette, Indiana 47907, USA*
[25]*Department of Physics and Astronomy, Rice University, Houston, Texas 77005, USA*
[26]*Department of Physics, University of California San Diego, La Jolla, California 92093, USA*
[27]*Kobayashi-Maskawa Institute for the Origin of Particles and the Universe, and Institute for Space-Earth Environmental Research, Nagoya University, Furo-cho, Chikusa-ku, Nagoya, Aichi 464-8602, Japan*
[28]*Department of Physics, School of Science, Westlake University, Hangzhou 310030, People's Republic of China*
[29]*Department of Physics, Kobe University, Kobe, Hyogo 657-8501, Japan*
[30]*INFN-Ferrara and Dipartimento di Fisica e Scienze della Terra, Università di Ferrara, 44122 Ferrara, Italy*
[31]*School of Science and Engineering, The Chinese University of Hong Kong (Shenzhen), Shenzhen, Guangdong, 518172, People's Republic of China*

(Received 9 October 2025; accepted 25 February 2026; published 2 April 2026)

We report the measurement of the ^{214}Bi β-decay spectrum to the ground state of ^{214}Po using the XENONnT detector. This decay is classified as first-forbidden nonunique, for which theoretical predictions require detailed nuclear structure modeling. A dedicated identification algorithm isolates a high-purity sample of ground-state β decays, explicitly excluding events with associated γ-ray emission. By comparing the measured spectrum, which covers energies up to 3.27 MeV, with several nuclear models, we find that the prediction based on the conserved vector current hypothesis provides the best description of the data. Using this dataset, we additionally derive charge and light yield curves for electronic recoils, extending detector response modeling up to the megaelectronvolt scale.

DOI: 10.1103/b3r7-6ff4

I. INTRODUCTION

Rare-event searches require a precise characterization of backgrounds in the signal region of interest. A ubiquitous source arises from radon, which emanates from detector materials containing trace amounts of uranium and thorium. Radon progeny undergoing β decay [1] constitute a major background, with ^{214}Pb and ^{214}Bi decays being key contributors in weakly interacting massive particle (WIMP) dark-matter searches [2–4] and neutrinoless double β-decay searches [5–7].

This study focuses on the ^{214}Bi β-decay spectral shape, whose decay scheme is shown in Fig. 1. The isotope ^{214}Bi has a half-life of 19.9 min, a Q value of 3.27 MeV, and a β-decay branching ratio of 99.979%, of which 19.2% decay directly into the ground state [8].

The Q value at $\mathcal{O}$(MeV) promotes the transition into excited states. The subsequent deexcitation leads to complex γ emission patterns. Theoretically, the multitude of accessible decay modes complicates the evaluation of the β spectrum, as calculations must account for a broad spectrum of nuclear transitions. Understanding the nuclear structure of isotopes like ^{214}Bi is crucial across various fields. One example is the modeling of the rapid neutron-capture process (r-process) [9], a key mechanism in stellar nucleosynthesis responsible for producing elements heavier than iron.

Experimentally, in a liquid-xenon TPC, β and γ interactions typically produce overlapping signals, which prevents separating the two components. However, a well-understood ^{214}Bi β spectrum would allow for a continuous detector calibration up to the β end point at 3.27 MeV, which is not possible with any other calibration sources.

In this study, we report a dedicated analysis in determining the ^{214}Bi ground-state spectrum using data from the XENONnT experiment [10]. Compared to the ^{214}Bi spectrum reconstruction by the NEMO experiment [11,12], the XENONnT detector has several advantages, including having an ultralow background and an *in situ* ^{222}Rn calibration. As the full ^{222}Rn decay process is contained within the XENONnT detector, the α decays and γ decays from the same decay chain are utilized to isolate the ^{214}Bi β decays. The selection algorithm developed in this work enables an effectively background-free measurement of the ^{214}Bi spectrum. Particular emphasis is placed on isolating the ground-state ^{214}Bi spectrum, allowing for direct comparisons with theoretical predictions. Furthermore, the XENON collaboration has developed a full-chain simulation framework, incorporating accurate detector response modeling. The simulation was adapted to develop the selection algorithm, while the ^{214}Bi data serves as a supporting benchmark for the simulation.

II. THEORETICAL FRAMEWORK

In β decay, the interaction is mediated by massive $W^{\pm}$ bosons between hadronic and leptonic currents. Assuming the decaying nucleon does not interact with the other $A-1$ nucleons, the probability density of the β-decay electron being

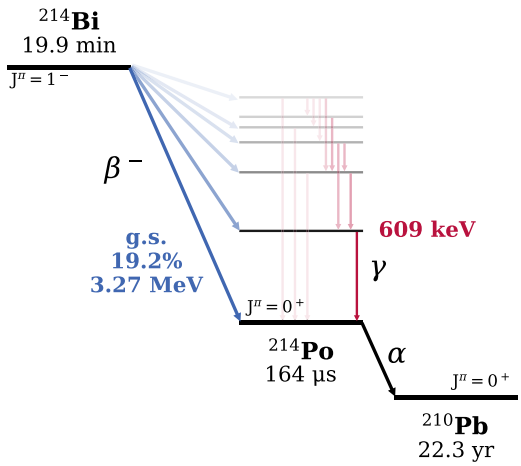

FIG. 1. Decay scheme of ^{214}Bi to ^{214}Po and subsequently to ^{210}Pb. The diagram shows β decays from ^{214}Bi (left) either directly to the ground state (g.s.) or via excited states of ^{214}Po (center). Approximately 80 excited nuclear states are accessible during the decay (symbolically represented). All these excited states deexcite via γ-decay emissions (red arrows), always including at least one transition greater than 609 keV. The final step is the α decay of ^{214}Po (black arrow) directly to the stable ground state of ^{210}Pb (right).

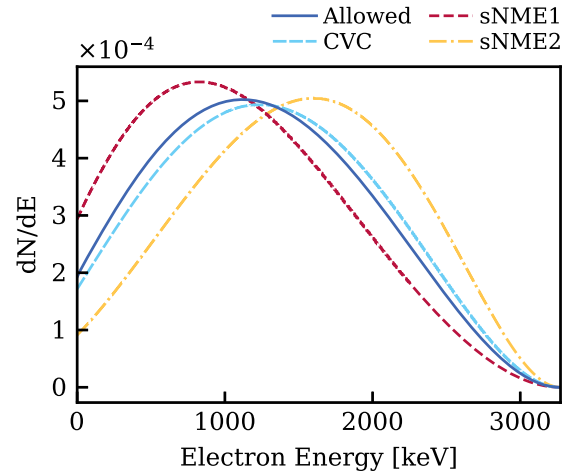

FIG. 2. Theoretical β-decay energy spectra for ground-state-to-ground-state transitions of ^{214}Bi to ^{214}Po. The solid blue line shows the *Allowed* spectrum, the dashed light blue line the *CVC*-based spectrum, the dashed red line the *sNME1* fit, and the dot-dashed yellow line the *sNME2* fit.

emitted with total energy E_e can be expressed as [13]

$$P(E_e)dE_e = \frac{G_F^2}{(\hbar c)^6}\frac{1}{2\pi^3\hbar}C(E_e) \times p_e c E_e (E_0 - E_e)^2 F_0(Z, E_e) dE_e, \quad (1)$$

where p_e is the momentum of the electron, E_0 the β-decay end-point energy, Z the proton number, G_F the Fermi constant, and $F_0(Z, E_e)$ the Fermi function. The nuclear structure information is encoded by the shape factor $C(E_e)$, which can generally be decomposed into vector, axial-vector, and mixed vector-axial-vector components:

$$C(E_e) = g_V^2 C_V(E_e) + g_A^2 C_A(E_e) + g_V g_A C_{VA}(E_e), \quad (2)$$

where g_V and g_A are the corresponding coupling constants for the vector and axial-vector components [1]. The contribution of the shape factors C_V, C_A, and C_{VA} is characterized by the nuclear matrix elements (NMEs).

The theoretical description of the β decay has undergone significant advancements in recent years, which have been essential for the background modeling of the XENON experiments [14,15], addressing the challenges when moving towards heavier nuclei and higher β-decay Q values. The complications include incorporating a large number of different transition modes in NMEs [16], modeling strong quenching of the weak-coupling constant g_A due to many-nucleon correlations [17] involving numerous approaches [18–22] and applying the mesonic enhancement correction from the effects of nuclear medium [23].

For the ^{214}Bi β decay, the transition to the ^{214}Po ground state proceeds from ^{214}Bi(1^-) to ^{214}Po(0^+), corresponding to a $\Delta J^\pi = 1^-$ change and therefore to a first-forbidden nonunique decay, which requires nondiagonal NMEs for its description [24]. The simplest reference is the zeroth-order spectrum, calculated analytically under the allowed approximation using the BETASHAPE software module [15] and shown in Fig. 2 as *Allowed*.

A more complete theoretical description is provided in Ref. [16], where the authors perform nuclear shell-model calculations for the atomic mass number $A \approx 214$ region using the KSHELL framework [25] to build the *khpe* Hamiltonian [26] and the NUSHELLX@MSU library [27] to extract single-particle energies considering relevant interaction and valence space. This produces the low-lying level schemes of ^{214}Bi and ^{214}Po to within tens of kiloelectronvolts, providing a reliable nuclear-structure basis for computing next-to-leading-order β-decay corrections under the conserved vector current (CVC) hypothesis, which enforces isospin symmetry, fixes the weak vector coupling to $g_V = 1.0$, and constrains the relevant vector form factors [28]. The resulting prediction is shown as the *CVC* spectrum in Fig. 2. Although CVC is well supported experimentally [29] and widely used in evaluations of forbidden shape factors [30], small deviations may arise from non-nucleonic effects [31]. The same study also introduced a complementary approach in which the small relativistic vector NMEs (sNMEs) are treated as fit parameters. By varying them simultaneously across all transitions to reproduce the experimental branching ratios, two degenerate solutions are obtained due to a quadratic dependence in the fit. These spectra, labeled *sNME1* and *sNME2*, are also taken from Ref. [16] and shown in Fig. 2. Together, the CVC and sNME spectra illustrate how modest variations in the vector NMEs can significantly alter the predicted ground-state β-decay spectrum, highlighting the need for an experimental determination.

III. EXPERIMENTAL METHOD

A. XENONnT detector and datasets

The XENONnT experiment [10] uses xenon as both the target and detection medium inside a cylindrical dual-phase

time projection chamber (TPC) that is 1.33 m in diameter and 1.49 m tall. The TPC contains 5.9 tonnes of liquid xenon (LXe), with a thin layer of gaseous xenon (GXe) at the top. An interaction with xenon atoms inside the TPC produces both prompt scintillation light, defined as the S1 signal, and ionization electrons. Meshed electrodes are used to apply an electric drift field in LXe (23 V/cm) and an extraction field in the region of the liquid-gas interface (2.9 kV/cm). This allows the free electrons to drift upward towards the LXe surface, where they are extracted into the GXe and generate secondary scintillation via electroluminescence, defined as the S2 signal. A total of 494 Hamamatsu R11410-21 photomultiplier tubes (PMTs) [32] are arranged at the top and bottom of the TPC to capture both the S1 and S2 signals, measured in units of photoelectrons (PE). A MeV electron in the TPC generates an S1 with a signal area of approximately 10^4 PE and an S2 of order 10^6 PE, while a MeV α generates an S1 of several 10^4 PE and an S2 of order 10^4 PE.

An event consists of a pair of S1 and S2 signals. The pairing enables reconstruction of the deposited energy and the three-dimensional interaction position, where the xy position is derived from the S2 scintillation photon hit pattern on the top PMT array and the z position from the time difference between S1 and S2. The position reconstruction permits the definition of a fiducial volume, selecting only the data from the interior of the TPC and thereby avoiding the background events originating from the decay of radioactive contaminants accumulated on the TPC wall. The dual signal also allows the discrimination between interactions with atomic electrons and with nuclei. The former is referred to as electronic recoil (ER) events, and the latter as nuclear recoils (NR) events. In dark-matter searches, WIMP signals have the NR signature. In this work, the ^{214}Bi β-decay signal of interest has the ER signature.

To achieve a minimal background, the XENONnT experiment is operated at the INFN Laboratori Nazionali del Gran Sasso underground laboratory. The cryostat containing the TPC is the innermost of three nested detectors. It is enclosed by a neutron veto [33] that is itself nested within a muon veto. Both veto detectors are water Cherenkov detectors and are optically separated. All detector construction materials were selected for low radioactivity [34]. The LXe is constantly purified via both gaseous and liquid purification systems [10] that remove electronegative impurities. The noble gas ^{85}Kr β-decay isotope, which is intrinsically present in xenon, was removed via a dedicated cryogenic distillation system [35] with the remnant measured [36]. For the radon background, a radon removal system also based on cryogenic distillation was installed to continuously remove the radon remnant from the TPC [37]. Finally, degreasing, etching, passivating, and screening were performed to ensure low radon emanation and electronegative impurities for all TPC components [34]. With all these background removal measures, XENONnT has achieved the lowest ever ER background among dark-matter detectors [38].

This study includes 95.1 days of data from the first science run (SR0) and 186.5 days from the second (SR1) of the XENONnT experiment. These datasets contain ^{214}Bi decays from natural ^{222}Rn emanation from detector materials at a ^{222}Rn rate of approximately 1.8 μBq/kg of LXe for SR0 and 1.0 μBq/kg for SR1 [39].

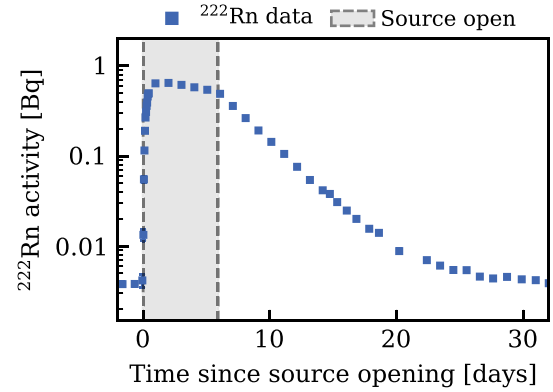

FIG. 3. Time evolution of the measured ^{222}Rn activity in the XENONnT TPC fiducial volume during the calibration campaign. The activity is derived from α decays, shown as a function of time since the source opening. The vertical dashed lines indicate the source opening and closing times.

To obtain sufficient statistics for this study, the most relevant XENONnT dataset is from a calibration campaign during SR1 using a ^{222}Rn source (SR1 ^{222}Rn). The source was produced by implanting ^{226}Ra into a 2 cm × 2 cm stainless steel plate at the ISOLDE facility at CERN [40], giving an overall emanated ^{222}Rn activity of about 2 Bq. The implantation is sufficiently deep below the surface, such that the ^{226}Ra atoms are mechanically sealed within the sample. Only the noble gas decay daughters ^{222}Rn are ejected from the sample.

During the ^{222}Rn (^{214}Bi) calibration period, the stainless steel sample was installed in-line with the gaseous purification system [10] and was flushed with GXe to carry the ^{222}Rn atoms to the xenon TPC. The time evolution of the source activity is tracked *in situ* via ^{222}Rn α decays as shown in Fig. 3. Shortly after the source injection, the ^{222}Rn activity increased by two orders of magnitude. Upon closing the source, the ^{222}Rn level decreased by a compound effect of the ^{222}Rn natural decay and the continuous operation of the radon removal system, returning the ^{222}Rn activity to the level observed before the calibration campaign. The expected level of long-term contamination, particularly from the β decay of ^{210}Pb (half-life 22.3 yr), which attaches to the TPC surfaces, has been evaluated as negligible.

We analyze the three datasets (SR0, SR1, SR1 ^{222}Rn) with independent treatments to account for their differences in operation and calibration conditions, before combining them into the final spectral data.

Finally, to accurately estimate the ER yield model *in situ*, we also utilized the XENONnT data from ^{220}Rn (^{212}Pb) calibrations [41].

B. Event topology

To select ^{214}Bi decays to the ^{214}Po ground state, we exploit the characteristic event topology. The delayed coincidence of a ^{214}Bi β decay, followed by the ^{214}Po α decay within the same chain is defined as ^{214}BiPo. Tagging an isolated ^{214}Bi β

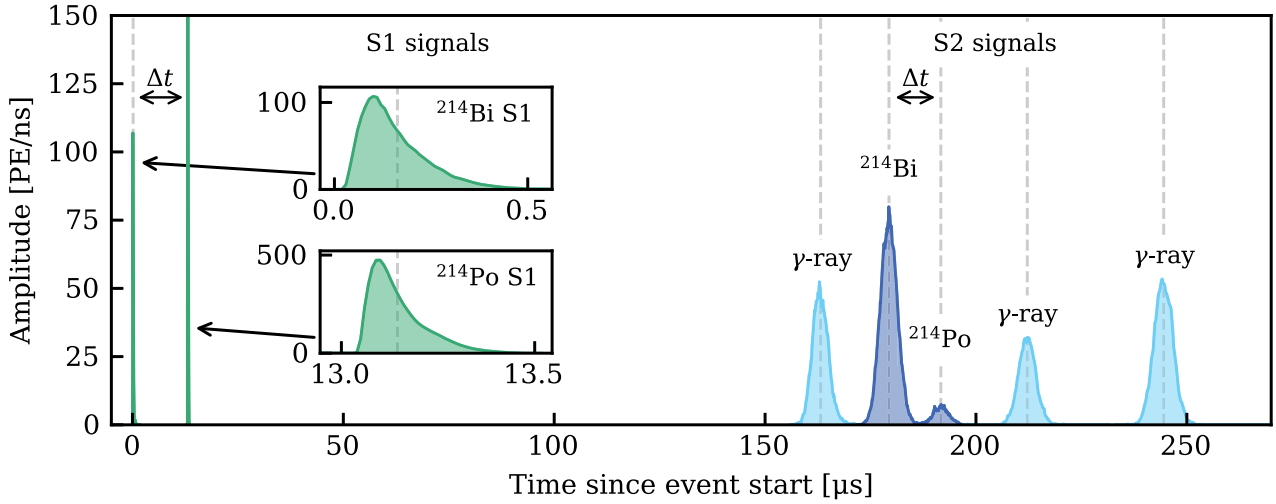

FIG. 4. Waveform representation of a typical ^{214}BiPo event from measured data. The two green peaks on the left correspond to the S1 signals of ^{214}Bi and ^{214}Po, separated by a time interval Δt. The two dark blue peaks on the right, also separated by Δt, are identified as the corresponding S2 signals. The light blue peaks represent S2 signals from γ emissions. Due to variations in electron drift distance, depending on whether the γ travels upward or downward, its S2 signal appears earlier or later than the ^{214}Bi S2. The α decay (^{214}Po) exhibits significant recombination and quenching effects, resulting in a smaller S2 despite its higher energy compared to the preceding β decay. Conversely, these effects enhance the S1 signal of the α decay. Inset panels show the S1 waveforms on an expanded timescale, highlighting their much shorter duration compared to S2 signals.

decay is inaccessible because of its broad spectrum and the presence of other ER background components. In contrast, the 7.83-MeV ^{214}Po α-decay [8] produces a prominent signal, with S1 signals of order 10^4 PE. The large S1 arises from the high stopping power of α particles, which create dense electron-ion tracks where recombination suppresses the S2 but enhances the S1 [42]. This tagging allows the determination of the α rate by isolating and counting the α events with negligible background. The derivation of the ^{222}Rn activity in Fig. 3, for instance, directly benefits from this tagging scheme. For the ^{214}Po α decays, they are especially well separated from the nearby α peaks by approximately 1 MeV. Moreover, the half-life of ^{214}Po is 164 μs [8], which is relatively short compared to the full TPC drift time of ∼2 ms and longer than the typical S2 signal width of ∼20 μs. In other words, we can use the ^{214}Po α to tag the ^{214}Bi decay in a ^{214}BiPo event with effectively no background.

The ^{214}BiPo event topology is illustrated in Fig. 4. The event is first triggered by the ^{214}Bi S1 signal and is shortly followed by a significantly larger S1 signal from ^{214}Po after a time difference of Δt. The S2s arrive a drift time later. The ^{214}Po S2 signal is suppressed as expected for an α event. The Δt is effectively preserved by the S2s because the α signals are localized in position: The ^{214}Po α particless travel on an order of 10 μm in LXe from the preceding ^{214}Bi decay.

A complication arises when considering the ^{214}Bi β decay into excited states that subsequently produce γ rays from nuclear deexcitation. Given that the deexcitation half-life is in the nanosecond range, the S1s of these γ rays are always merged with the S1 of the β. However, unlike α particles, the γ rays can travel a few centimeters before interacting with another xenon atom [43]. This shift in positions of the interaction site results in ^{214}BiPo events with more than two S2s, as illustrated in Fig. 4. Notably, however, among all the deexcitation γ rays of the ^{214}Bi β decay as illustrated in Fig. 1, there is always one γ photon with an energy at least 609 keV. We can effectively use these high-energy γ decays to tag the excited states.

C. Event selection

This analysis relies on the ^{214}BiPo *tagging algorithm*, a method that exploits the time coincidence between the ^{214}Bi β decay and the subsequent α decay of ^{214}Po. Although ^{214}BiPo tagging is commonly employed in low-background experiments [11,44,45], our implementation specifically addresses the complexity introduced by γ emissions accompanying ^{214}Bi decays into excited nuclear states. These emissions produce events with multiple signals, complicating straightforward time-based matching. To reliably pair the correct S1 and S2 signals, our algorithm compares the time differences Δt between all combinatoric pairs formed by the three largest S1 signals (to account for possible spurious signals) and up to 10 largest S2 signals. We identify events in which one S1 pair and one S2 pair have matching Δt values within a tolerance of ±3 μs. Peaks from S2 signals with areas below 1500 PE, unphysical top-bottom PMT area distributions, or inappropriate timing (such as spurious pulses that occur shortly after the main pulse and can be reconstructed as separate peaks), are excluded from the matching procedure. We use simulations, described in Sec. III D, to quantify the matching efficiency, which is >91% for true ground-state events, providing validation of the matching approach.

Following the matching procedure, we apply a series of *quality selection criteria* to ensure high-quality event

reconstruction and minimize contributions from backgrounds or poorly reconstructed signals. Events must pass the fiducial volume constraint, defined by a vertical depth at least 5 cm away from the top and bottom boundaries of the TPC to avoid regions with field inhomogeneities [46]. A minimum separation of 25 µs between the two primary S1 signals is required to prevent potential merging of the corresponding S2 signals, given a typical S2 width at 90% of the area of up to 20 µs. This criterion results in only a modest loss of approximately 3% of events, as shorter S1 intervals typically produce merged, unresolved S2 signals. This requirement also eliminates the background contribution of ^{212}BiPo events originating from the ^{220}Rn decay chain, with a similar topology as the ^{214}BiPo but with a half-life of 300 ns. Additional criteria based on the α S1 signal area are employed to remove events originating from other α decays. These selection steps reduce the dataset to approximately 165 000 events, which include both ground-state and excited-state decays.

The final *ground-state selection* step specifically isolates ^{214}Bi decays directly to the ^{214}Po ground state. We require exactly two S2 signals above 1500 PE, corresponding to the β decay and the subsequent α decay. To suppress events with additional γ interactions, any third S2 is required to be smaller than 10 000 PE. This selection effectively excludes most excited-state decays, which, due to selection rules, deexcite through high energy γ decays leading to clearly identifiable additional S2 signals. Although further criteria, such as a selection on the S2 width to remove partially merged signals, were tested, they provided no significant improvement beyond the initial matching procedure. This selection yields 56 965 events, corresponding to 31% of the events that passed the quality criteria.

Using detailed simulations (described in Sec. III D), we evaluate the performance and purity of the selection procedure. After applying matching and quality criteria, the requirement of precisely two S2 signals achieves a signal acceptance of around 94% (the fraction of true ground-state events passing the final selection) and a background rejection of approximately 93% (the fraction of excited-state events removed by the selection).

The fraction of excited-state events that pass the ground-state selection criteria (approximately 20% of the total selected events) predominantly belongs to two categories of roughly equal proportions. The first category consists of events in which the emitted γ rays completely escape the active detection volume. These events are reconstructed at energies lower than genuine ground-state events, as only the energy deposited by the β electron is observed. The second category comprises events where γ-induced signals fully merge with the β electron signals, resulting in artificially higher reconstructed energies due to the combined γ and β contributions. A much smaller additional contribution arises from internal conversion (IC): In these transitions, the γ ray is replaced by the emission of an orbital electron, followed by Auger electrons and x-rays from atomic-shell rearrangement. Because this energy is deposited locally, IC events do not provide spatially separated interactions that are characteristic of γ rays and therefore offer limited separation power. The expected IC fraction for the most relevant transitions is at the percentage level and is fully accounted for in the GEANT4 simulation. All three contributions are included in the modeling of leakage events used in the comparison between data and simulation.

D. Simulations and signal modeling

Simulations for this analysis are produced using the XENONnT framework [47], which incorporates a full-chain simulation from energy deposition to final event reconstruction. Initial interactions, including both the ^{214}Bi and subsequent ^{214}Po decays, are simulated with Geant4 [48,49]. This step considers all relevant nuclear decay characteristics, including the full decay scheme of ^{214}Bi, associated branching ratios, and emitted γ energies. To investigate different theoretical models of the ^{214}Bi ground-state β-decay spectrum introduced in Fig. 2, we adjusted the input β energy distribution provided to Geant4 accordingly, creating simulation datasets for each considered model.

Subsequent stages of the simulation that include clustering of deposited energies, generation and propagation of photons and electrons using detector-specific efficiency maps, electron drifting, and waveform simulation are performed using the fuse package [47]. These simulated waveforms closely replicate those recorded by the data acquisition system of the XENONnT detector, allowing for the use of an identical processing pipeline as for the real data with the straxen package [50].

For accurate modeling of events with energies up to 3.27 MeV, which is substantially higher than the typical range targeted by the dark-matter search analyses (<100 keV) [51], we extended the existing fuse framework with a specialized simulation workflow. Two critical improvements were implemented: a more physically motivated clustering algorithm for energy depositions and a data-driven yield model specifically tailored for high-energy electron recoils. The latter describes the photon and electron yields per unit energy.

Clustering of energy depositions is necessary because the data-driven yield models, such as the ones provided by NEST [52,53], require input energies to attribute the correct amount of photons and electrons generated by individual interactions. Due to the incomplete understanding of the underlying microphysics at these scales, energy depositions must be aggregated into physically meaningful clusters before applying the yield model. The default clustering method used in XENONnT [51] groups energy depositions solely based on spatial and temporal proximity. While adequate at lower energies, this method is inadequate in describing complex high-energy event topologies. The new framework employs a lineage clustering method inspired by NEST, which groups interactions based on their physical properties and interaction history. Energy depositions from electron tracks are grouped into single clusters, except for Bremsstrahlung photons, which form separate clusters. Gamma interactions instead initiate new clusters for each distinct interaction site, effectively differentiating γ from β events.

Unlike the default NEST model, which employs separate yield models for gamma and β interactions, our approach uses a single, unified yield model. The apparent difference

between the two cases originates from the underlying physics: interactions of γ rays via Compton scattering lead to energy depositions at multiple spatially separated sites, while electrons typically deposit all energy in a contained interaction cluster. Each site contributes its own cluster with energy E_i, and since the charge and light yields depend nonlinearly on E_i, the combined yield of these clusters differs from that of a single deposition with the same total energy. In our analysis, this distinction emerges naturally from clustering: The yield difference between β decays and γ decays is not imposed through separate models but arises directly from the physical interaction topology when combined with the clustering method.

We extract a new parametrization of the ER yield model using single β-decay events, which provide well-defined single-cluster energy depositions. For this purpose, we use ^{212}Pb decays from ^{220}Rn calibrations together with SR0 ^{214}Bi decays from this analysis, ensuring broad coverage across the full energy range. The yield parameters are obtained by fitting the 10-parameter NEST function [52] to the measured charge yield, with the light yield calculated as the complementary fraction of quanta.

We account for residual leakage of excited-state events into the ground-state selection by comparing yields in simulation from truth-level ground-state β-decay events with those obtained when the excited-state events that passed the selection are included. The observed difference is implemented as an effective correction to the charge and light yield in data. Since the leakage events concentrate above 1.8 MeV, this region is excluded from the fit.

Figure 5 compares the resulting charge and light yield curves with both the default NEST model at a drift field of 23 V/cm and the official XENONnT yield model used for low-energy searches [51]. The latter, derived from ^{37}Ar and ^{212}Pb calibrations, is in good agreement with our parametrization below 20 keV. The NEST model, although nominally valid at the megaelectronvolt scale, is largely based on data below 100 keV. Moreover, only limited experimental input exists at the drift field of XENONnT (23 V/cm), making the extrapolation in this regime uncertain and leading to clear discrepancies in charge and light yields.

To account for the fact that the energy bias correction described in the next section acts on the reconstructed energy but not on S1 and S2 independently, we include in Fig. 5 a systematic uncertainty band on our yield curves. The shaded band reflects the propagation of the energy bias into the extracted yields, covering the systematic uncertainty introduced by peak reconstruction and subsequent energy determination.

We validated the resulting yield model using two independent datasets: the clean single-cluster β selection described above, and the ^{214}BiPo events including excited-state decays that produce combined β and γ topologies. These events, with multiple interaction sites and complex clustering, provide a stringent test of the clustering and yield framework. Although the yield parameters were derived only from clean β decays below 1.8 MeV, the model reproduces the measured S1 and S2 distributions at the percentage level across the full energy range, up to the ^{214}Bi end point. By contrast, simulations based on the default NEST yields and spatial

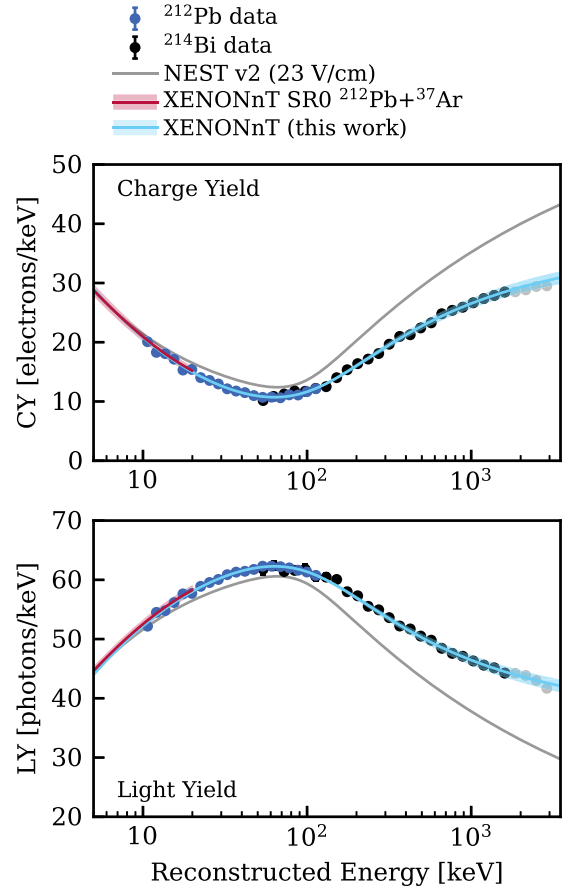

FIG. 5. Charge yield (CY, top) and light yield (LY, bottom) as a function of reconstructed energy, extracted from β decays of ^{212}Pb (blue) and ^{214}Bi (black). The ER yield model (light blue) is obtained by fitting the charge yield, with the light yield derived as the complementary fraction of total quanta. The shaded band accounts for the systematic uncertainty from the energy-bias correction. A correction for residual excited-state leakage is applied to the data. Grayed-out ^{214}Bi points above 1.8 MeV are excluded from the fit due to γ contamination. For comparison, the default NEST model at 23 V/cm (gray) and the XENONnT low-energy yield model (red) are shown. Statistical uncertainties are smaller than the marker size.

clustering showed discrepancies of up to 50% in S2 for $\beta + \gamma$ events above a few hundred kiloelectronvolts. The agreement obtained here therefore supports the changes in both the clustering method and the yield parametrization: Reproducing multicluster topologies at high energy is only possible if both components are accurate.

The clustering procedure and yield parametrization introduced above are designed specifically to achieve accurate reproduction of the individual S1 and S2 distributions between data and simulations. They do not directly guarantee agreement in the reconstructed energy spectra, which is instead addressed in the following section through dedicated corrections.

E. Energy bias correction

To ensure consistent energy reconstruction across simulations and the three experimental datasets (SR0, SR1, and SR1 ^{222}Rn), we derive dataset-specific energy-dependent bias corrections, addressing known effects described in previous XENONnT analyses [51]. These biases affect both the S1 and S2 signals, primarily arising from electronic noise, PMT response effects, afterpulses, photoionization, and threshold effects from the data acquisition system and ancillary software thresholds.

To accurately compare true energies, we first reconstruct the energy for each event as

$$E_{\mathrm{rec}} = W \cdot \left(\frac{cS1}{g_1} + \frac{cS2}{g_2} \right), \tag{3}$$

where $W = 13.7$ eV [54] is the average energy required to produce one quantum (photon or electron) in liquid xenon, cS1 and cS2 are the corrected S1 and S2 signals, and g_1 and g_2 are detector-specific calibration constants determined from the data [51]. In this analysis, we use the following values that were determined in earlier XENONnT analyses. For SR0 we adopt $g_1 = 0.151$ PE/photon and $g_2 = 16.5$ PE/electron [51]; for SR1, we use $g_1 = 0.1367$ PE/photon and $g_2 = 16.9$ PE/electron [2].

Following the procedure described in Ref. [51], we then define an empirical energy correction for each dataset by measuring the bias using monoenergetic peaks from background and calibration sources. For each peak, the bias is calculated using $\Delta E = (E_{\mathrm{rec}} - E_{\mathrm{true}})$ and fitted with an arctan function:

$$F(E_{\mathrm{rec}}) \equiv \frac{\Delta E}{E_{\mathrm{rec}}} \times 100 = A \cdot \arctan(kE_{\mathrm{rec}}) + c, \tag{4}$$

where A, k, and c are free fit parameters.

We use monoenergetic lines from ^{37}Ar (2.8 keV), ^{83m}Kr (41.5 keV), ^{131m}Xe (163.9 keV), ^{129m}Xe (236.1 keV), electron-positron annihilation (511 keV), ^{60}Co (1173.2 keV and 1332.5 keV), and γ rays from external[1] ^{214}Bi (1764.5 keV), and ^{208}Tl (2614.5 keV). For SR1, the ^{37}Ar line originates from an accidental injection of commercial-grade xenon into the detector before the start of SR1. The ^{37}Ar was removed using cryogenic distillation before the ^{222}Rn calibration, so no ^{37}Ar datapoint is available in the SR1 ^{222}Rn dataset. For simulations, monoenergetic γ rays and electrons at different energies were uniformly simulated throughout the detector volume.

Figure 6 shows the fitted bias curves for each dataset, exhibiting clear differences: SR0 is calibrated such that ^{37}Ar has zero bias by construction, while SR1 shows systematically lower biases, becoming negative at low energies. The SR1 ^{222}Rn calibration data display higher biases at higher energies. We attribute the overall offset of the curves mainly to different choices in the g_1 and g_2 determination procedure, while the increase in amplitude with energy is governed by detector conditions such as the higher event rate during calibrations and photoionization, where absorbed photons release additional delayed electrons. Because no ^{37}Ar anchor point is available in the SR1 ^{222}Rn dataset, the fit was performed under constraints to prevent unphysical divergence. For this reason, we do not show the uncertainty band for this dataset in Fig. 6, as the unconstrained errors would be unrealistically large. This choice does not affect the analysis: The lowest energy bin used in the spectrum study is at 65 keV, well above the missing ^{37}Ar line.

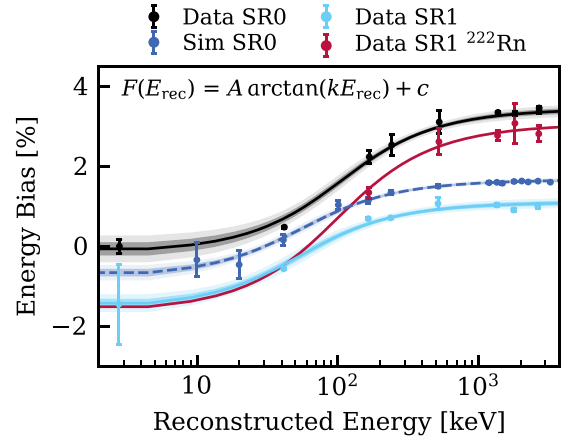

FIG. 6. Energy bias as a function of reconstructed energy for SR0 (black), SR1 (cyan), and SR1 ^{222}Rn calibration data (red), as well as SR0 simulations (blue dashed). The data points correspond to monoenergetic calibration peaks at known energies. The uncertainties on each point correspond to the uncertainty in the mean obtained from the Gaussian fit to the energy distribution of the selected peaks. Bias values are fitted with an arctangent function, and shaded bands indicate the 1σ and 2σ confidence intervals of the fit. Uncertainty bands for the ^{222}Rn dataset are omitted for clarity.

The best-fit parameters for each dataset are reported in the Appendix.

IV. RESULTS

A. Models to data comparison

In this analysis, the event selection is rendered effectively free of background contamination as a result of the ^{214}BiPo identification algorithm. The primary remaining background arises from γ leakage from excited-state decays into the ground-state selection. Since this leakage is accurately modeled by our simulations, which incorporate well-measured γ emissions from ^{214}Bi, we can compare data directly to full-chain simulations.

We combine data from the three experimental datasets: SR0 (7708 events), SR1 (5542 events), and the SR1 ^{222}Rn (37 835 events). The consistency of the ratio between quality-selected and ground-state-selected events across these datasets (∼30%) allows combining them into a single dataset. The energies of each dataset have been individually corrected for the energy bias described in Sec. III E.

[1]External ^{214}Bi refers to the ^{214}Bi produced in the uranium decay chain within the construction materials. In this case, only the γ ray can reach the TPC, while the accompanying electron is absorbed before entering the detector and remains undetected.

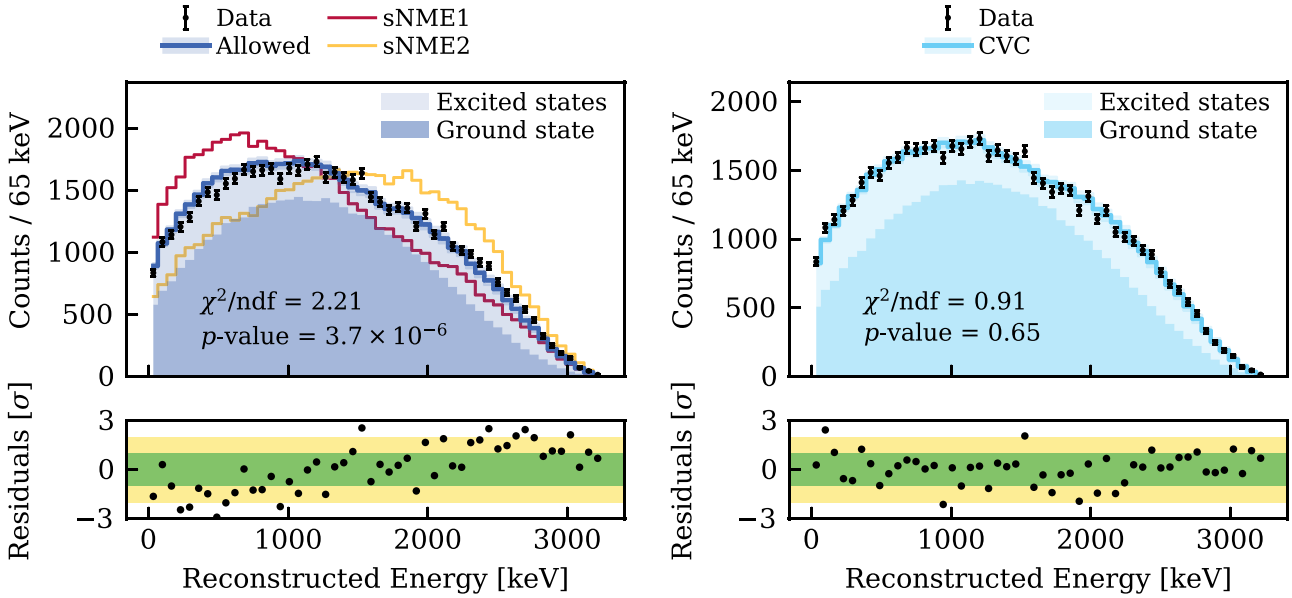

FIG. 7. Detailed comparison of the measured energy spectrum of ^{214}Bi ground-state data with simulations. Left panel: Data compared with the allowed model (filled histogram), including the true ground-state and excited-state contributions. The sNME1 and sNME2 theoretical spectra are shown as thin lines for reference. Right panel: Comparison with the CVC spectrum (filled histogram). The normalized residuals with respect to the allowed (left) and CVC (right) spectra are displayed in the bottom panels, along with the corresponding reduced chi-squared (χ^2/ndf) and p values.

Figure 7 presents the combined dataset in comparison with four simulation sets corresponding to the different theoretical β-decay spectra: *Allowed*, *CVC*, *sNME1*, and *sNME2*. The simulated spectra are normalized to match the total number of events observed in data; this normalization involves no free fitting parameters, ensuring a robust, unbiased comparison of spectral shapes. Statistical and systematic uncertainties are included in the simulations, as discussed in Sec. IV B, whereas the data points represent purely statistical uncertainties.

The sNME1 and sNME2 models exhibit significant discrepancies from the measured spectrum and are excluded from further consideration. The allowed model shows a clear energy-dependent deviation visible in the residuals (bottom panel), indicating a systematic mismatch. On the other hand, the CVC spectrum provides an excellent description of the data, with a high p value larger than 0.05 and no evident residual energy trend. This comparison strongly favors the CVC spectrum as the most accurate theoretical description of our data.

B. Systematic uncertainties

We address potential systematic uncertainties arising from mismatches between simulation and data, particularly those with energy-dependent effects. We identify and evaluate three primary sources of uncertainty.

First, we consider uncertainties due to γ-event leakage into the β selection. While waveform properties like the S1/S2 amplitudes and signal widths are well matched between simulations and data, slight mismatches could still affect the fraction of excited-state events leaking into the ground-state selection. To account for this, we apply a 1% variation to the total number of leakage events. This choice is motivated by the observed stability (within 1%) of the ratio of selected ground-state events to all quality-selected events across multiple datasets.

Second, we examine uncertainties related to the energy scale of excited-state events. While γ energies are well known from precise nuclear spectroscopy, the associated β spectra are more difficult to measure and model. To assess the stability of the result, we apply an effective 5% energy shift to all excited-state events. This corresponds to approximately 150 keV at the β end point, compatible with the spectral shifts observed in the ground-state spectrum studied in this work. The effect on the reconstructed spectrum is limited by the relatively small contribution of excited-state events and the dominant role of the well-measured γ energies.

Finally, we evaluate the overall energy scale uncertainty. The reconstructed energy is corrected using energy-bias curves derived from calibration peaks, for which the fitted peak positions have uncertainties below 0.25%. To account for possible residual effects, we apply a conservative 0.5% global energy shift. At the β end point, this corresponds to a less than 20 keV shift, which is smaller than the bin widths.

These three sources of uncertainty were combined by evaluating their impact on the simulated energy spectrum in each energy bin. The resulting variations were added in quadrature and incorporated as an additional uncertainty on the simulated prediction, on top of the statistical uncertainties from data. The combined systematic uncertainty remains below 1% across the entire energy range and is subdominant to the statistical error. In the high-energy tail, where event statistics are low, systematic and statistical effects become correlated, but statistical uncertainties dominate.

V. CONCLUSION AND OUTLOOK

We presented a measurement of the energy spectrum of the ^{214}Bi β decay to the ground state of ^{214}Po using data from the XENONnT experiment. The event selection employs a dedicated ^{214}BiPo tagging technique, combining background data with a ^{222}Rn calibration campaign. By developing an improved high-energy simulation pipeline, we successfully modeled ER signals up to 3.27 MeV, well beyond the low-energy range defined for WIMP searches. Our analysis strongly favors the theoretical spectrum calculated under the CVC hypothesis, significantly rejecting the allowed approximation and alternative nuclear models. These results demonstrate the capability of dual-phase xenon detectors to perform high-precision β spectroscopy, providing valuable validations for theoretical predictions and reinforcing their potential for probing nuclear processes relevant to fundamental physics and astrophysics.

ACKNOWLEDGMENTS

We thank X. Mougeot, M. Ramalho, and J. Suhonen for kindly sharing data and for valuable discussions.

We thank ISOLDE team at CERN for assisting in carrying out the implantation for the ^{222}Rn source.

We gratefully acknowledge support from the National Science Foundation, Swiss National Science Foundation, German Ministry for Education and Research, Max Planck Gesellschaft, Deutsche Forschungsgemeinschaft, Helmholtz Association, Dutch Research Council (NWO), Fundacao para a Ciencia e Tecnologia, Weizmann Institute of Science, Binational Science Foundation, Région des Pays de la Loire, Knut and Alice Wallenberg Foundation, Kavli Foundation, JSPS Kakenhi, JST FOREST Program, and ERAN in Japan, Tsinghua University Initiative Scientific Research Program, National Natural Science Foundation of China, DIM − ACAV+ Région Ile-de-France, and Istituto Nazionale di Fisica Nucleare. This project has received funding/support from the European Union's Horizon 2020 and Horizon Europe research and innovation programs under the Marie Skłodowska-Curie Grants No. 860881-HIDDeN and No. 101081465-AUFRANDE.

We gratefully acknowledge support for providing computing and data-processing resources of the Open Science Pool and the European Grid Initiative, at the following computing centers: the CNRS/IN2P3 (Lyon, France), the Dutch national e-infrastructure with the support of SURF Cooperative, the Nikhef Data-Processing Facility (Amsterdam, Netherlands), the INFN-CNAF (Bologna, Italy), the San Diego Supercomputer Center (San Diego, USA), and the Enrico Fermi Institute (Chicago, USA). We acknowledge the support of the Research Computing Center (RCC) at The University of Chicago for providing computing resources for data analysis.

We thank the INFN Laboratori Nazionali del Gran Sasso for hosting and supporting the XENON project.

DATA AVAILABILITY

The data that support the findings of this article are not publicly available. The data are available from the authors upon reasonable request.

APPENDIX A: YIELDS PARAMETERS

We summarize the best-fit parameters for the ER yield model obtained from fitting ^{212}Pb and ^{214}Bi calibration data in XENONnT. The model defines the charge yield as

$$Q_y(E,\mathcal{E}) = m_1(\mathcal{E}) + \frac{m_2 - m_1(\mathcal{E})}{\left[1+\left(\frac{E}{m_3(\mathcal{E})}\right)^{m_4(\mathcal{E})}\right]^{m_9}} + m_5(\mathcal{E}) - \frac{m_5(\mathcal{E})}{\left[1+\left(\frac{E}{m_7(\mathcal{E})}\right)^{m_8}\right]^{m_{10}(\mathcal{E})}}, \quad \text{(A1)}$$

where E is the energy of the interaction and $\mathcal{E}$ is the electric field. The parameters $m_1 - m_{10}$ are described in detail in Ref. [53].

Our best-fit values, reported in Table I, differ notably from the default NEST values, particularly in the high-energy region (m_5, m_8, m_{10}), highlighting the need for a data-driven recalibration for accurate high-energy ER modeling in XENONnT.

TABLE I. Fit results for the NEST ER yield model parameters.

Parameter	Description	Fit value	NEST Default (23 V/cm)
m_1	Stitching-region yield	5.00 ± 0.24	7.10
m_2	Low-energy asymptote	83 ± 3	77.3
m_3	Thomas-Imel shape control	2.00 ± 0.06	0.716
m_4	Low-energy shape control	0.77 ± 0.03	1.83
m_5	High-energy asymptote	29.3 ± 0.7	48.6
m_7	High-energy scaling	125.4 ± 2.2	94.4
m_8	High-energy shape control	2.21 ± 0.08	4.29
m_9	Low-energy asymmetry control	1.072 ± 0.006	0.334
m_{10}	High-energy asymmetry control	0.29 ± 0.09	0.066

TABLE II. Energy bias fit results.

Dataset	A	k	c
SR0	2.30 ± 0.12	0.0095 ± 0.0013	−0.2 ± 0.2
SR1	1.70 ± 0.09	0.018 ± 0.003	−1.56 ± 0.13
SR1 ^{222}Rn	3 ± 7	0.01 ± 0.03	−2 ± 12
Simulations	1.56 ± 0.07	0.018 ± 0.002	−0.79 ± 0.12

APPENDIX B: ENERGY BIAS FIT RESULTS

In Table II we report the parameters obtained from the fits of the energy bias function described in Sec. III E. The function and the parameters are introduced in Eq. (4). The reported best-fit values can be used to reproduce the bias correction curves shown in Fig. 6 for SR0, SR1, SR1 ^{222}Rn, and the SR0 simulation dataset.

[1] R. P. Feynman and M. Gell-Mann, Theory of Fermi interaction, Phys. Rev. **109**, 193 (1958).

[2] E. Aprile, *et al.* (XENON Collaboration), WIMP dark matter search using a 3.1 tonne-year exposure of the XENONnT experiment, Phys. Rev. Lett. **135**, 221003 (2025).

[3] J. Aalbers, *et al.* (LZ Collaboration), Dark matter search results from 4.2 tonne-years of exposure of the LUX-ZEPLIN (LZ) experiment, Phys. Rev. Lett. **135**, 011802 (2025).

[4] Z. Bo, *et al.* (PandaX Collaboration), Dark matter search results from exposure of PandaX-4T, Phys. Rev. Lett. **134**, 011805 (2025).

[5] E. Aprile, *et al.* (XENON Collaboration), Double-weak decays of ^{124}Xe and ^{136}Xe in the XENON1T and XENONnT experiments, Phys. Rev. C **106**, 024328 (2022).

[6] S. A. Kharusi, *et al.* (EXO Collaboration), Search for two-neutrino double-beta decay of ^{136}Xe to the excited state of ^{136}Ba with the complete EXO-200 dataset, Chin. Phys. C **47**, 103001 (2023).

[7] S. Abe, *et al.* (KamLAND-Zen Collaboration), Search for Majorana neutrinos with the complete KamLAND-Zen dataset, Phys. Rev. Lett. **135**, 262501 (2025).

[8] S.-C. Wu, Nucl. Data Sheets for A = 214, Nucl. Data Sheets **110**, 681 (2009).

[9] M. Arnould, S. Goriely, and K. Takahashi, The r-process of stellar nucleosynthesis: Astrophysics and nuclear physics achievements and mysteries, Phys. Rep. **450**, 97 (2007).

[10] E. Aprile, *et al.* (XENON Collaboration), The XENONnT dark matter experiment, Eur. Phys. J. C **84**, 784 (2024).

[11] R. Arnold, *et al.* (NEMO-3 Collaboration), Results of the search for neutrinoless double-β decay in ^{100}Mo with the NEMO-3 experiment, Phys. Rev. D **92**, 072011 (2015).

[12] A. S. Barabash, *et al.* (SuperNEMO Collaboration), The BiPo-3 detector for the measurement of ultra low natural radioactivities of thin materials, J. Instrum. **12**, P06002 (2017).

[13] E. D. Commins, *Weak Interactions* (McGraw–Hill, New York, 2007).

[14] S. J. Haselschwardt, J. Kostensalo, X. Mougeot, and J. Suhonen, Improved calculations of β decay backgrounds to new physics in liquid xenon detectors, Phys. Rev. C **102**, 065501 (2020).

[15] X. Mougeot, BetaShape: A new code for improved analytical calculations of beta spectra, in *EPJ Web Conference* (EDP Sciences, Bruges, Belgium, 2016), Vol. 146, p. 12015.

[16] M. Ramalho and J. Suhonen, Computed total β-electron spectra for decays of Pb and Bi in the ^{220,222}Rn radioactive chains, Phys. Rev. C **109**, 014326 (2024).

[17] Q. Zhi, E. Caurier, J. J. Cuenca-García, K. Langanke, G. Martínez-Pinedo, and K. Sieja, Shell-model half-lives including first-forbidden contributions for r-process waiting-point nuclei, Phys. Rev. C **87**, 025803 (2013).

[18] F. F. Deppisch and J. Suhonen, Statistical analysis of β decays and the effective value of g_A in the proton-neutron quasiparticle random-phase approximation framework, Phys. Rev. C **94**, 055501 (2016).

[19] J. Kostensalo and J. Suhonen, g_A-driven shapes of electron spectra of forbidden β decays in the nuclear shell model, Phys. Rev. C **96**, 024317 (2017).

[20] J. Toivanen and J. Suhonen, Microscopic quasiparticle-phonon description of odd-mass isotopes and their β decay, Phys. Rev. C **57**, 1237 (1998).

[21] E. Caurier, F. Nowacki, and A. Poves, Shell model description of the $\beta\beta$ decay of ^{136}Xe, Phys. Lett. B **711**, 62 (2012).

[22] F. Iachello and P. V. Isacker, *The Interacting Boson-Fermion Model* (Cambridge University Press, New York, 1991).

[23] J. Kostensalo and J. Suhonen, Mesonic enhancement of the weak axial charge and its effect on the half-lives and spectral shapes of first-forbidden $j^+ \leftrightarrow j^-$ decays, Phys. Lett. B **781**, 480 (2018).

[24] H. Ejiri, J. Suhonen, and K. Zuber, Neutrino–nuclear responses for astro-neutrinos, single beta decays and double beta decays, Phys. Rep. **797**, 1 (2019).

[25] N. Shimizu, T. Mizusaki, Y. Utsuno, and Y. Tsunoda, Thick-restart block Lanczos method for large-scale shell-model calculations, Comput. Phys. Commun. **244**, 372 (2019).

[26] E. K. Warburton and B. A. Brown, Appraisal of the Kuo-Herling shell-model interaction and application to $A = 210$–212 nuclei, Phys. Rev. C **43**, 602 (1991).

[27] B. A. Brown and W. D. M. Rae, The shell-model code NuShellX@MSU, Nucl. Data Sheets **120**, 115 (2014).

[28] H. Behrens and W. Bühring, *Electron Radial Wave Functions and Nuclear Beta-decay*, International Series of Monographs on Physics (Clarendon Press, Oxford, 1982).

[29] J. C. Hardy and I. S. Towner, New limits on fundamental weak-interaction parameters from superallowed β decay, Phys. Rev. Lett. **94**, 092502 (2005).

[30] A. Kumar, P. C. Srivastava, and J. Suhonen, Second-forbidden nonunique β^- decays of ^{59,60}Fe: Possible candidates for g_a sensitive electron spectral-shape measurements, Eur. Phys. J. A **57**, 225 (2021).

[31] M. Haaranen, J. Kotila, and J. Suhonen, Spectrum-shape method and the next-to-leading-order terms of the β-decay shape factor, Phys. Rev. C **95**, 024327 (2017).

[32] V. C. Antochi, *et al.*, Improved quality tests of R11410-21 photomultiplier tubes for the XENONnT experiment, J. Instrum. **16**, P08033 (2021).

[33] E. Aprile, *et al.* (XENON Collaboration), The neutron veto of the XENONnT experiment: Results with demineralized water, Eur. Phys. J. C **85**, 695 (2025).

[34] E. Aprile, *et al.* (XENON Collaboration), Material radiopurity control in the XENONnT experiment, Eur. Phys. J. C **82**, 599 (2022).
[35] E. Aprile, *et al.* (XENON Collaboration), Application and modeling of an online distillation method to reduce krypton and argon in XENON1T, Prog. Theor. Exp. Phys. **2022**, 053H01 (2022).
[36] S. Lindemann and H. Simgen, Krypton assay in xenon at the ppq level using a gas chromatographic system and mass spectrometer, Eur. Phys. J. C **74**, 2746 (2014).
[37] E. Aprile, *et al.* (XENON Collaboration), Online ^{222}Rn removal by cryogenic distillation in the XENON100 experiment, Eur. Phys. J. C **77**, 358 (2017).
[38] M. Murra, D. Schulte, C. Huhmann, C. Weinheimer, *et al.*, Design, construction and commissioning of a high-flow radon removal system for XENONnT, Eur. Phys. J. C **82**, 1104 (2022).
[39] E. Aprile, *et al.* (XENON Collaboration), Radon removal in XENONnT down to the solar neutrino level, Phys. Rev. X **15**, 031079 (2025).
[40] F. Jörg, G. Eurin, and H. Simgen, Production and characterization of a ^{222}Rn-emanating stainless steel source, Appl. Radiat. Isot. **194**, 110666 (2023).
[41] E. Aprile, *et al.* (XENON Collaboration), Results from a calibration of XENON100 using a source of dissolved radon-220, Phys. Rev. D **95**, 072008 (2017).
[42] F. Jörg, D. Cichon, G. Eurin, L. Hötzsch, T. M. Undagoitia, and N. Rupp, Characterization of alpha and beta interactions in liquid xenon, Eur. Phys. J. C **82**, 361 (2022).
[43] M. J. Berger, J. H. Hubbell, S. M. Seltzer, J. Chang, J. S. Coursey, R. Sukumar, D. S. Zucker, and K. Olsen, XCOM: Photon cross section database (version 1.2) (1999), https://physics.nist.gov/xcom.
[44] E. Aprile, *et al.* (XENON Collaboration), Offline tagging of radon-induced backgrounds in XENON1T and applicability to other liquid xenon time projection chambers, Phys. Rev. D **110**, 012011 (2024).
[45] A. Gando, *et al.* (KamLAND-Zen Collaboration), Search for Majorana neutrinos near the inverted mass hierarchy region with KamLAND-Zen, Phys. Rev. Lett. **117**, 082503 (2016).
[46] E. Aprile, *et al.* (XENON Collaboration), Design and performance of the field cage for the XENONnT experiment, Eur. Phys. J. C **84**, 138 (2024).
[47] H. Schulze Eißing, *et al.* (XENON Collaboration), XENONnT/fuse: 1.4.2, Zenodo (2025), https://doi.org/10.5281/zenodo.14740249.
[48] S. Agostinelli, *et al.* (GEANT4 Collaboration), GEANT4—A simulation toolkit, Nucl. Instrum. Methods A **506**, 250 (2003).
[49] J. Allison, *et al.*, Geant4 developments and applications, IEEE Trans. Nucl. Sci. **53**, 270 (2006).
[50] J. R. Angevaare, *et al.* (XENON Collaboration), XENONnT/straxen: v3.1.4, Zenodo (2025), https://doi.org/10.5281/zenodo.14996117.
[51] E. Aprile, *et al.* (XENON Collaboration), XENONnT analysis: Signal reconstruction, calibration, and event selection, Phys. Rev. D **111**, 062006 (2025).
[52] M. Szydagis, N. Barry, K. Kazkaz, J. Mock, D. Stolp, M. Sweany, M. Tripathi, S. Uvarov, N. Walsh, and M. Woods, NEST: A comprehensive model for scintillation yield in liquid xenon, J. Instrum. **6**, P10002 (2011).
[53] M. Szydagis, *et al.*, A review of NEST models for liquid xenon and an exhaustive comparison with other approaches, Front. Detect. Sci. Technol. **2**, 1480975 (2025).
[54] E. Aprile, C. E. Dahl, L. DeViveiros, R. Gaitskell, K. L. Giboni, J. Kwong, P. Majewski, K. Ni, T. Shutt, and M. Yamashita, Simultaneous measurement of ionization and scintillation from nuclear recoils in liquid xenon as target for a dark matter experiment, Phys. Rev. Lett. **97**, 081302 (2006).